

The stratified disk wind of MCG-03-58-007

V. Braito^{1,2*}, J. N. Reeves^{1,2}, P. Severgnini¹, R. Della Ceca¹,
L. Ballo³, C. Cicone⁴, G. A. Matzeu^{1,3}, R. Serafinelli¹, M. Sirressi⁵

¹INAF - Osservatorio Astronomico di Brera, Via Bianchi 46 I-23807 Merate (LC), Italy & Via Brera 28, 20121, Milano

²Department of Physics, Institute for Astrophysics and Computational Sciences, The Catholic University of America, Washington, DC 20064, USA

³European Space Astronomy Centre (ESA/ESAC), E-28691 Villanueva de la Canada, Madrid, Spain

⁴Institute of Theoretical Astrophysics, University of Oslo, P.O. Box 1029 Blindern, 0315 Oslo, Norway

⁵Department of Astronomy, AlbaNova University Center, Stockholm University, SE-10691 Stockholm, Sweden

Accepted XXX. Received YYY; in original form ZZZ

ABSTRACT

Past *Suzaku*, *XMM-Newton* and *NuSTAR* observations of the nearby ($z = 0.03233$) bright Seyfert 2 galaxy MCG-03-58-007 revealed the presence of two deep and blue-shifted iron K-shell absorption line profiles. These could be explained with the presence of two phases of a highly ionized, high column density accretion disk wind outflowing with $v_{\text{out1}} \sim -0.1c$ and $v_{\text{out2}} \sim -0.2c$. Here we present two new observations of MCG-03-58-007: one was carried out in 2016 with *Chandra* and one in 2018 with *Swift*. Both caught MCG-03-58-007 in a brighter state ($F_{2-10\text{ keV}} \sim 4 \times 10^{-12} \text{ erg cm}^{-2} \text{ s}^{-1}$) confirming the presence of the fast disk wind. The multi-epoch observations of MCG-03-58-007 covering the period from 2010 to 2018 were then analysed. These data show that the lower velocity component outflowing with $v_{\text{out1}} \sim -0.072 \pm 0.002c$ is persistent and detected in all the observations, although it is variable in column density in the range $N_{\text{H}} \sim 3 - 8 \times 10^{23} \text{ cm}^{-2}$. In the 2016 *Swift* observation we detected again the second faster component outflowing with $v_{\text{out2}} \sim -0.2c$, with a column density ($N_{\text{H}} = 7.0^{+5.6}_{-4.1} \times 10^{23} \text{ cm}^{-2}$), similar to that seen during the *Suzaku* observation. However during the *Chandra* observation two years earlier, this zone was not present ($N_{\text{H}} < 1.5 \times 10^{23} \text{ cm}^{-2}$), suggesting that this faster zone is intermittent. Overall the multi-epochs observations show that the disk wind in MCG-03-58-007 is not only powerful, but also extremely variable, hence placing MCG-03-58-007 among unique disk winds such as the one seen in the famous QSO PDS456. One of the main results of this investigation is the consideration that these winds could be extremely variable, sometime appearing and sometime disappearing; thus to reach solid and firm conclusions about their energetics multiple observations are mandatory.

Key words: galaxies: active – galaxies: individual (MCG-03-58-007) – X-rays: galaxies

1 INTRODUCTION

Less than twenty years after the discovery of the first examples of highly-ionized ($\log(\xi/\text{erg cm s}^{-1}) = 3 - 6$), massive and fast ($v > 0.1c$) outflowing absorbers (PDS 456, Reeves et al. 2003, PG1211+143, Pounds et al. 2003 and APM08279+5255, Chartas et al. 2002), it is now largely accepted that fast disk winds are commonly observed in nearby bright AGN (Tombesi et al. 2010, 2012; Gofford et al. 2013, 2015). Although a lot of observational and theoretical effort has been invested in understanding their nature and their possible role in shaping the host galaxies (King 2010; King et al. 2011; Nardini & Zubovas 2018 and references therein), several questions still remain open including their main driving mechanism, their variability and their real impact on the host galaxy. The velocities measured for these winds can reach up to $\sim 0.3c$ (PDS 456 Reeves et al. 2009, 2014, APM08279+5255 Chartas et al. 2002), suggesting that they most likely originate in the innermost region of the accretion disk (see King & Pounds 2015) and there-

fore could be linked to the accretion process itself (King & Pounds 2003; King 2010; King & Pounds 2015). They could be driven either by the radiation pressure (Proga et al. 2000; Proga & Kallman 2004; Sim et al. 2008, 2010), by magneto-rotational forces (MHD models: Kato et al. 2004; Kazanas et al. 2012; Fukumura et al. 2010, 2017) or a combination of both.

The measured relativistic velocities and high column densities imply that, although affected by high uncertainties, the outflow rates and kinetic output can be huge and match or exceed the conventional threshold of $L_{\text{KIN}}/L_{\text{bol}} \sim 0.5 - 5\%$ for an efficient AGN feedback on the host galaxy (Hopkins & Elvis 2010; Di Matteo et al. 2005). These disk winds might indeed drive the massive molecular outflows seen on kpc-scales (Cicone et al. 2014, 2015; Fiore et al. 2017) and thus influence the host galaxies by sweeping away the interstellar medium and suppressing star formation (King & Pounds 2015; Zubovas & King 2012, 2016). Thus these disk winds could play a major role in the feedback process that shapes the formation of the stellar bulges and simultaneously self regulate the growth of the super massive black hole (SMBH), leading to the observed AGN-host galaxy relationships like the $M - \sigma$ relation (Magorrian et al.

* E-mail: valentina.braito@brera.inaf.it

1998; Ferrarese & Merritt 2000; Gebhardt et al. 2000).

The first detections of powerful X-ray disk winds in two Ultra Luminous Infrared Galaxies (ULIRGs), where massive large-scale molecular outflows are also present (Mrk 231; Feruglio et al. 2015 and IRAS F11119+3257; Tombesi et al. 2015) seemed to support a scenario where the molecular outflows are driven by an energy conserving disk wind. Here, when the disk wind propagates and shocks with the ISM it does not cool efficiently and the large-scale outflow receives a momentum boost (King 2010; Faucher-Giguère & Quataert 2012). However, recent results on other ultra fast disk winds observed with the Atacama Large Millimeter/submillimeter Array (ALMA) show that not all outflows lie on the energy conserving relation. Actually, with the more recent IRAM and ALMA data, only Mrk 231 and IRAS 17020+4544 (Longinotti et al. 2018) are consistent with the above scenario. An energy conserving wind can be clearly ruled out for both the prototype of the fast disk winds PDS 456 (Bischetti et al. 2019) and the powerful wind of IZw 1 (Reeves & Braito 2019). This hints for a range of efficiencies in transferring the kinetic energy of the inner wind out to the large-scale molecular component (Mizumoto et al. 2019), which suggest that the role of the powerful disk winds in the galaxy evolution may be more complex than what we thought. Several scenarios can indeed explain the lack of a powerful molecular outflow; among them the large scale gas could be clumpy as seen in the ALMA observation of PDS456 (Bischetti et al. 2019) or it could be ionized. Furthermore, once we consider that the typical dynamical timescales of the large scale outflows are of the order of $t \sim 10^6 - 10^7$ yr, it is not unexpected that we do not observe the two phases simultaneously. Indeed, there could be a substantial delay between the onset of the fast X-ray wind and the large-scale energy conserving wind (King et al. 2011).

It is clear that, if we want to establish the role of the AGN disk winds at driving the large scale outflows, we need more examples of disk winds in conjunction with multiwavelength observations of the host galaxies, which can reveal the large-scale component of the outflows, as well as further investigate the most compelling cases of X-ray disk winds. First of all it is essential to establish if the fast wind is persistent or not, then we need to refine the measurement of the persistent component of the wind, so that we do not introduce an error on the estimates of the mass and energetics of the disk wind. We note, that with the exception of PDS 456, the variability of the X-ray disk winds is poorly studied. In the best studied examples the fast disk wind can be variable in ionisation, column density (N_H) and even velocity (e.g. PDS 456, Reeves et al. 2018a; Matzeu et al. 2017; IRAS F11119+3257, Tombesi et al. 2017; PG 1211+143, Reeves et al. 2018b and APM08279+5255, Saez & Chartas 2011). This observational evidence is in agreement with disk wind simulations where the stream is not expected to be a homogeneous and constant flow (Proga & Kallman 2004; Giustini & Proga 2012). The observed variations could be either explained with our line of sight intercepting different clumps or streams of the winds or with a response of the wind to the luminosity of the X-ray source. Recently, a direct correlation between the outflow velocity and the intrinsic ionising luminosity was reported for PDS 456 (Matzeu et al. 2017), IRAS 13224-3809 (Chartas & Canas 2018) and APM08279+5255 (Saez & Chartas 2011), while a correlation between the ionisation of the disk wind and the X-ray luminosity was reported for IRAS 13224-3809 by Pinto et al. (2018). This indicates the importance of the incident radiation upon the wind: as the luminosity and thus the radiation pressure increases, a faster wind is driven.

MCG-03-58-007 is a bright and nearby Seyfert 2 galaxy ($F_{2-10\text{keV}} \sim 2 \times 10^{-12} \text{ erg cm}^{-2} \text{ s}^{-1}$, $z = 0.03233$; Sirressi et al. 2019). The first deep *Suzaku* (Mitsuda et al. 2007) observation per-

formed in 2010 showed a spectrum of an obscured AGN ($N_H \sim 2 \times 10^{23} \text{ cm}^{-2}$) and, surprisingly, two deep ($EW \sim 300 \text{ eV}$) blue-shifted absorption troughs at $E = 7.4 \pm 0.1 \text{ keV}$ and $E = 8.5 \pm 0.2 \text{ keV}$ (Braito et al. 2018, hereafter B18). These are most likely associated with two zones of a highly ionized ($\log(\xi/\text{erg cm s}^{-1}) \sim 5.5$) and high column density ($N_H \sim 5 - 8 \times 10^{23} \text{ cm}^{-2}$) outflowing wind with $v_{\text{out}1} \sim -0.1 c$ and $v_{\text{out}2} \sim -0.2 c$. The derived kinetic output ($\dot{E}_k \sim 2.4 \times 10^{44} \text{ erg s}^{-1}$) is $\sim 8\%$ of the bolometric luminosity (or $\sim 2\%$ of L_{Edd}), placing MCG-03-58-007 among the most powerful disk winds. A deep follow-up observation was carried out in 2015 with *XMM-Newton* & *NuSTAR* (of ~ 130 ksec net exposure each). This follow-up confirmed the presence of the slow component of the wind, but did not confirm the $\sim 8.5 \text{ keV}$ feature previously observed in the *Suzaku* spectra. This observation unveiled also a possible faster ($v_{\text{out}} \sim -0.35 c$) component of the wind. Remarkably, during this *XMM-Newton* & *NuSTAR* observation we witnessed an X-ray eclipse caused by a denser ($\Delta N_H \sim 10^{24} \text{ cm}^{-2}$) streamline of the wind moving across our line of sight that lasted $\Delta t \sim 120$ ksec, which is outflowing at $v_{\text{out}} \sim -0.124 c$. A further investigation of the broad band X-ray emission, performed adopting a more self-consistent model for the pc-scale toroidal absorber (MYTORUS, Murphy & Yaqoob 2009) confirmed that the short-term X-ray spectral variability cannot be accounted for by N_H variations of the neutral absorber, but certainly requires a variable highly ionized fast wind (Matzeu et al. 2019, hereafter M19).

MCG-03-58-007 was also observed with ALMA, revealing a component that likely corresponds to a low velocity ($v_{\text{CO}} \sim 170 \text{ km s}^{-1}$) molecular outflow in the central 4 kpc. However, as for PDS 456 and IZw 1 (Reeves & Braito 2019), the kinetic power of the putative molecular outflow is at least two orders of magnitude below the expected value for an energy conserving wind ($\dot{E}_{\text{Mol}}/\dot{E}_X \sim 4 \times 10^{-3}$; Sirressi et al. 2019).

Here we present the results of two follow-up observational campaigns performed with *Chandra* in 2016 and with *Swift* in 2018, both of which caught MCG-03-58-007 in a brighter state ($F_{2-10\text{keV}} \sim 3.7 \times 10^{-12} \text{ erg cm}^{-2} \text{ s}^{-1}$). We will show that the slowest component of the wind is persistent, as it is detected in all the observations with a similar velocity of $v_{\text{out}} \sim -0.07 c$ and it is variable in column density, confirming its clumpy nature. On the contrary the second component of the wind seen during the *Suzaku* observation appears more sporadic. The paper is structured as follows: in §2 we briefly summarise the previous *Suzaku*, *XMM-Newton* & *NuSTAR* observations, which were already discussed in B18 and in M19. The data reduction of the *Swift* and *Chandra* observations is also presented in detail in §2. In §3 we present the spectral modelling focusing on the variability of the wind components. The discussion of the disk wind and the implications of the long term variability are presented in §4. Throughout the paper we assume a concordance cosmology with $H_0 = 70 \text{ km s}^{-1} \text{ Mpc}^{-3}$, $\Omega_{A_0} = 0.73$ and $\Omega_m = 0.27$. For the abundances we used those of Wilms et al. (2000).

2 OBSERVATIONS AND DATA REDUCTION

2.1 Earlier observations: *Suzaku*, *XMM* and *NuSTAR*

MCG-03-58-007 was observed in the X-ray band in four epochs with five different satellites; in Table 1 we report the observation dates, instruments and the net exposure times for the all the available observations.

Table 1. Summary of the observations used: Observatory, Observation Date, Instrument, Elapsed and Net exposure times. The net exposure times are obtained after the screening of the cleaned event files.

| Mission | Start Date (UT Time) | Instrument | Elapsed Time (ks) | Exposure _(net) (ks) |
|-------------------|----------------------|------------|-------------------|--------------------------------|
| <i>Suzaku</i> | 2010-06-03 16:50 | XIS | 187.4 | 87.0 |
| <i>XMM-Newton</i> | 2015-12-06 12:15 | EPIC-pn | 131.3 | 59.9 |
| <i>NuSTAR</i> | 2015-12-06 10:36 | FPMA | 281.8 | 131.4 |
| <i>Chandra</i> | 2016-09-25 05:14 | ACIS-S | 44 | 39.8 |
| <i>Chandra</i> | 2016-09-20 09:23 | ACIS-S | 17 | 15.5 |
| <i>Swift</i> | 2018-04-15 13:22 | XRT | - | 19.6 |
| <i>Swift</i> | 2018-04-19 00:27 | XRT | - | 17.6 |
| <i>Swift</i> | 2018-04-20 00:29 | XRT | - | 6.1 |
| <i>Swift</i> | 2018-04-22 03:28 | XRT | - | 19.7 |
| <i>Swift</i> | 2018-04-23 23:58 | XRT | - | 3.0 |
| <i>Swift</i> | 2018-04-25 03:01 | XRT | - | 3.8 |

For the *Suzaku*, *XMM-Newton* and *NuSTAR* observations we adopt the same spectra as already described in detail in B18 and M19. As per the previous analysis, the *XMM-Newton* & *NuSTAR* observations were split into two main intervals: slice A and slice B (see Fig. 5 of B18), where slice A is the relatively unobscured half of the observation and slice B is where MCG-03-58-007 dropped in flux and appeared to go into a more obscured state (see B18 and M19 for details). For simplicity, here we considered only the EPIC-pn spectrum as the agreement with the MOS spectrum is already discussed in M19. In this analysis we combined the *NuSTAR* FPMA and FPMB spectra, because the individual detectors were consistent, and then grouped the resulting spectrum to reach at least 50 total counts per bin. For these two epochs we will limit our analysis to the best fits obtained in the previous works and simply test a new grid of photoionised absorbers (see below).

2.2 Chandra

MCG-03-58-007 was observed with *Chandra* in September 2016; the observation was split into two shorter exposures (see Table 1) that were carried out five days apart. The observations were performed with the Advanced CCD Imaging spectrometer (ACIS-S; [Garmire et al. 2003](#)) in the 1/8 sub-array mode. We reduced the data with the Chandra Interactive Analysis of Observation software (CIAO v. 4.10; [Fruscione et al. 2006](#)) and the latest Chandra Calibration Data Base (CALDB version 4.8.1). We followed the standard reduction procedures and extracted source and background spectra using a circular region of 2.5'' and 4.5'' radius, respectively. We then inspected the spectra extracted from the two exposures and verified that there was no evidence for strong spectral variability and only a moderate flux variation between the two spectra ($\sim 15\%$). We thus added the spectra and combined the responses files with appropriate weighting. The resulting spectrum was then binned to a minimum of 20 total counts per bin and modelled over the 0.5 – 9 keV energy range.

We also extracted soft (0.5–2 keV) and hard (2–8 keV) X-ray images. We first corrected the absolute astrometry of the images adjusting the aspect solution file and the event file astrometry with the CIAO tools *wcs_update* and *reproject_events*. We then merged the event files of the two observations using the CIAO tool *dmerge*. Soft and hard X-ray images were then created using a binning at 1/8 of the native pixel size and then adaptively smoothed using the tool *dmimgadapt*, which assumes a gaussian function with sigma values ranging from 1

to 30 image pixels and a minimum convolution kernel of 2 counts¹. The inspection of the images shows that most of the X-ray emission originates in the innermost 1'' (or ~ 650 pc), with only a weak residual soft X-ray emission extending up to $\sim 4''$ (see Fig. 1). This is in agreement with the RGS spectral analysis presented in M19, where the soft X-ray emission was attributed to the presence of gas that is mainly photoionised by the central AGN and possibly associated with the emission of the circumnuclear Narrow Line Region gas.

2.3 Swift

Swift observed MCG-03-58-007 in 2018 for a total exposure time of ~ 70 ksec. The observational campaign consisted of six XRT exposures in the standard PC-mode, with three long (~ 19 ksec each) exposures and three shorter observations (see Table 1). The observations were performed as a monitoring program aimed at investigating the possible variability of the neutral absorber on time scales as short as a day. The observations were performed in April 2018 covering about 10 days.

We extracted the source and background spectra from each of the observations adopting a circular region with a radius of 42'' and 78'', respectively. We also extracted broadband as well as soft (0.3–2 keV) and hard (2–10 keV) X-ray light curves and found no evidence for spectral variability and only minor flux variations within $\sim 20\%$. The inspection of the spectra extracted from all the observations suggests that MCG-03-58-007 was caught in a similar state in each of them. Before adding all the six spectra, we fitted all of them with a baseline continuum model composed of: an absorbed power component, a scattered power-law emission and a thermal emission component, finding consistent spectral parameters and only moderate flux variations. We also note that the residuals of all three longest observations show a drop above 7 keV. However, the low count statistics in the individual spectra prevent us from investigating the nature of the drop in the single observations, therefore we combined all of them into a single spectrum. We then binned the combined spectrum to a minimum of 20 total counts per bin and considered the 0.3 – 9 keV energy range for the following spectral analysis.

¹ For details see: <https://cxc.cfa.harvard.edu/ciao/ahelp/dmimgadapt.html>

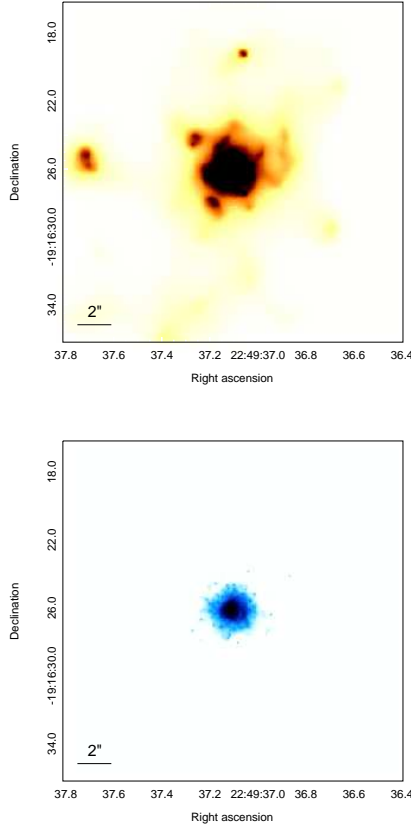


Figure 1. Upper Panel: *Chandra* soft (0.5-2 keV) image ($20'' \times 20''$) of MCG-03-58-007. The soft X-ray emission is mostly concentrated in the central nuclear region (within $2''$) with some weak emission extending up to almost $4''$. The spatial scale is reported at the bottom right (note that for MCG-03-58-007 $1''$ correspond to ~ 650 pc). Lower panel: hard (3-8 keV) X-ray image of MCG-03-58-007. The hard X-ray emission is close to a point like appearance and originates from the inner $1''$. We used a subpixeling factor of eight to create the images, thus the pixel size is 0.062 arcsec. The images were adaptively smoothed with *dmimadap*.

3 SPECTRAL ANALYSIS

3.1 Baseline model

In Fig. 2 we show the fluxed spectra of all the X-ray observations, obtained by unfolding the data against a power law model with $\Gamma = 2$. Two facts emerge by comparing all the observations. First of all, the spectral curvature, that we can ascribe to the presence of the neutral absorber, appears to be similar in all the spectra, with the exception of the second part of the *NuSTAR* observation (slice B, see Fig. 2, dark blue spectrum). Second and more importantly all the spectra show a drop around $7.2 - 7.4$ keV. We also note that in the two new observational campaigns (Fig. 2, red and black data points for the *Chandra* and *Swift* spectra, respectively) we caught MCG-03-58-007 in a relatively brighter state ($F_{(2-10) \text{ keV}} \sim 3.7 \times 10^{-12} \text{ erg cm}^{-2} \text{ s}^{-1}$; see Table 2).

The best fit model found for the first two epochs (e. g. B18) was defined as:

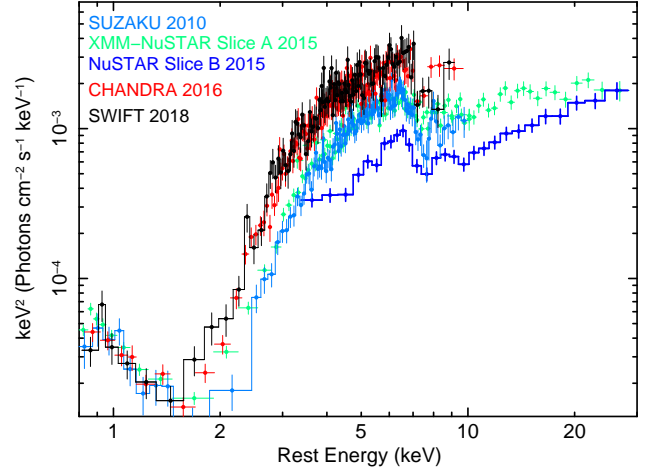


Figure 2. Fluxed spectra of all the recent X-ray observations of MCG-03-58-007 showing the short (on timescale of a day) and long term variability of the X-ray emission. The *Suzaku* spectrum (collected in 2010) is shown in light blue. The *XMM-Newton* & *NuSTAR* simultaneous observation performed in 2015 (slice A) are shown in green. The second half of the *NuSTAR* observation (slice B), where the eclipsing event occurred, is shown in blue. The spectra collected during the most recent observations performed with *Chandra* in 2016 and *Swift* in 2018 (average) are shown in red and black, respectively. To generate the plot, we created fluxed spectra by unfolding the data against a $\Gamma = 2$ power law model. The data have been rebinned for plotting purposes.

$$F(E) = \text{TBABS} \times [\text{ZPOW}_{\text{scatt}} + \text{XSTAR}_{\text{em}} + \text{MEKAL} + \text{PEXMON} \\ + \text{ZPHABS} \times \text{XSTAR}_{\text{FeK},1} \times \text{XSTAR}_{\text{FeK},2} \times \text{ZPOW}]$$

Here *TBABS* represents the neutral Galactic absorption ($N_{\text{H}} = 2.5 \times 10^{20} \text{ cm}^{-2}$; [Dickey & Lockman 1990](#)), *ZPOW_{scatt}* is the scattered power-law component; the cold reflection component is modelled with *PEXMON* ([Nandra et al. 2007](#)), which includes also the Fe $K\alpha$, Fe $K\beta$ and the Ni $K\alpha$ emission lines as well as the Fe $K\alpha$ Compton shoulder. We fixed the inclination angle to 60 degrees and the high energy cutoff to 100 keV. We fixed also the amount of reflection $R = \Omega/2\pi = 1$, while the normalisation is allowed to vary. For the reflection component we tied its photon index Γ to the primary power-law component, while we allow the scattered power-law component to have a different slope to account for any soft excess. For the soft X-ray emission the best fit models include both the emission from a collisionally ionized plasma (*MEKAL* component, with $kT = 0.84 \pm 0.08$ keV) and the optically thin gas photoionized by the AGN (*XSTAR_{em}*; see M19). Finally, *XSTAR_{FeK,1}* and *XSTAR_{FeK,2}* are the two photoionised absorbers.

We first proceeded to fit the new *Chandra* and *Swift* spectra with the best fit continuum model found for the previous observations, minus the two photoionised absorbers. In Fig. 3 we show the residuals in the iron absorption region of all the spectra to the baseline continuum model, where for completeness we also report the residuals of the previous *Suzaku* and *XMM-Newton* & *NuSTAR* spectra. For simplicity for the 2015 observation, here we only show the *XMM-pn* data of slice A. A similar comparison between slice A and the slice B residuals is shown in Fig. 8 of B18. We note that for the *XMM-Newton* & *NuSTAR* spectra (both slice A and slice B) we included a neutral reflection component to the baseline continuum model (as above), which we modelled with the *PEXMON*

component allowing only its normalisation to vary. For the *Chandra* & *Swift* datasets, which lack the bandpass above 10 keV, this is not required. Two main facts emerge when inspecting the residuals. First of all a trough at $\sim 7.2 - 7.6$ keV appears to be present in all the observations, albeit it may vary in depth; as we investigate below this may be ascribed to the variable lower velocity zone of the disk wind. The second fact that emerges is that a higher energy absorption structure is seen at ~ 8.5 keV in only two of the four epochs, the *Suzaku* and *Swift* spectra.

We then reapplied the best fit model, which includes two multiplicative grids of ionised absorption models, to the previous *Suzaku*, *XMM-Newton* & *NuSTAR* spectra (both slice A and slice B) and also to the new *Chandra* and *Swift* observations. We considered each observation separately, with the exception of the *Chandra* & *Swift* observations, which caught MCG-03-58-007 with a similar continuum and flux level, where we tied only the main parameters of the continuum, but we allowed the N_H of two ionised absorbers to be independent from each other. We assumed for all the observations the same photon index as currently measured with *NuSTAR* ($\Gamma = 2.17 \pm 0.06$, see Table 2), because we lack any coverage above 10 keV, where the primary continuum emission emerges. We note that the Γ derived here is marginally different from the one reported by M19 for a similar configuration (Model A in M19: $\Gamma = 2.25 \pm 0.07$); however it is well within the errors. Similarly to what was found by M19, when the photon index of the soft scattered component is allowed to vary it tends to a high value ($\Gamma_{\text{soft}} = 3.7 \pm 0.3$). However, the precise modelling of the soft X-ray emission does not affect the parameters of the neutral absorber or of the disk wind (see also M19).

A difference of the fits presented here is that to model the two zones disk wind we generated a new grid of photoionised absorbers with the *xstar* photoionisation code (Kallman et al. 2004). The grid was generated assuming a high turbulence velocity ($v_{\text{turb}} = 10^4 \text{ km s}^{-1}$). We assumed a SED similar to IZW1, where the soft (between 0.3 and 1.2 keV) photon index (Γ) is ~ 3 and the hard X-ray Γ is 2.2 (see Reeves & Braito 2019). This is justified by the fit reported by M19, where the soft X-ray slope was indeed of the order of 3, in agreement with the slope measured here (see above). The grid was optimised for high column density ($N_H = 10^{22} - 2 \times 10^{24} \text{ cm}^{-2}$) and high ionisation ($\log(\xi/\text{erg cm s}^{-1}) = 3 - 7$) absorbers. The main difference to the grid used in the previous works is that this new grid has finer steps² (i. e. it interpolates between a larger number of ionized absorbers). The choice of the high turbulence velocity is justified by the broadening measured for the absorption features. For instance, if we model the two absorption features seen in the *Suzaku* spectra with two Gaussian absorption lines, we measure $\sigma \sim 0.35 \pm 0.08 \text{ keV}$ (or $\sigma \sim 1.4 \times 10^4 \text{ km s}^{-1}$, see also B18). Nevertheless, we also tested grids with a lower turbulence velocity (i. e. $v_{\text{turb}} = 1 - 5 \times 10^3 \text{ km s}^{-1}$), which resulted in worse fits. In particular, for $v_{\text{turb}} = 1000 \text{ km s}^{-1}$ the fit of the *Suzaku* spectra is worse by $\Delta\chi^2 = 31.4$; the predicted absorption features are too narrow and cannot reproduce the breadth and depth of the observed profiles. Note that, as discussed in B18, the equivalent widths of the absorption lines seen in the *Suzaku* spectra is of the order of $\sim 300 \text{ eV}$. Another difference with the previous fits is that here we assumed the ionisation of the two zones to be the same.

In Table 2, we report the new parameters obtained for these observations, using the new grid of models.

² The *xstar* grid was generated with 20 linear steps for ξ and 10 logarithmic steps for N_H .

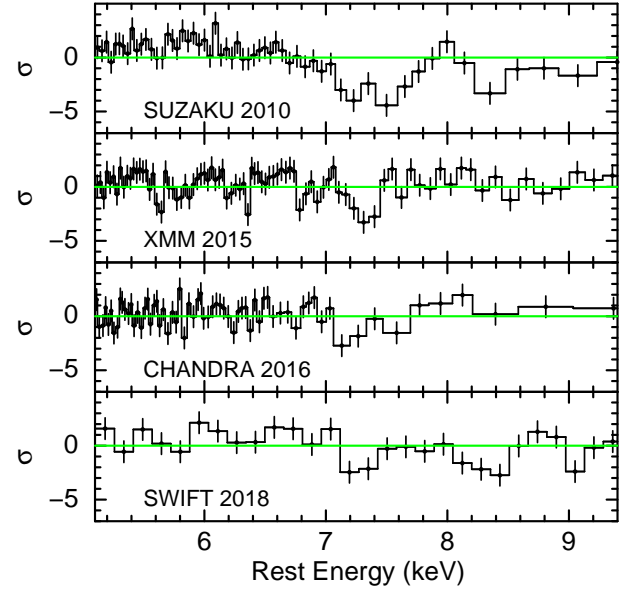


Figure 3. Residuals for all the observations to the continuum model where we assumed the same photon index for the primary power law component. The continuum model is composed by a soft power-law component, a collisionally and a photoionized plasma emission components and a primary power-law component transmitted through a neutral absorber. For the 2015 *XMM-Newton* & *NuSTAR* observation we include also a reflection component modelled with *peخمون* (Nandra et al. 2007). The $\sim 7.4 \text{ keV}$ absorption trough is at its weakest during the *XMM*-slice A. It is also apparent that, while a higher energy absorption trough is present at $\sim 8.5 \text{ keV}$ in the 2010 and 2018 spectra it is undetected in the 2015 *XMM* and 2016 *Chandra* observations. The *Swift* data are binned adopting a constant energy bin of 150 eV for plotting purposes.

3.2 Slower outflow component

Given the known degeneracy between N_H and $\log \xi$, we proceeded to investigate the variability of the Fe K absorption troughs by allowing only the column density to vary and assumed a constant ionisation (see below). We also allowed the outflow velocity to vary between the observations.

In Table 2 we summarise the results of the best fits for each of the datasets. The inclusion of the first zone of the wind improves all the fits for a $\Delta\chi^2/\Delta\nu = 107.5/3$, $\Delta\chi^2/\Delta\nu = 27.2/3$ and $\Delta\chi^2/\Delta\nu = 17.3/3$ for the *Suzaku*, slice A & slice B and the *Chandra* & *Swift* data, respectively.

We found that, with the exception of the obscured slice B, the outflow velocity is consistent within errors over all the epochs, ranging from $v_{\text{out1}}/c \sim -0.072$ to $v_{\text{out1}}/c \sim -0.077$, while the column density of this lower velocity zone varies among all of the observations. The wind opacity is at its maximum level during the *Suzaku* observation in 2010 ($N_H = 8.1^{+3.0}_{-2.4} \times 10^{23} \text{ cm}^{-2}$; see Table 2) and it is at its lowest level in slice A with a measured $N_H = 2.6^{+1.1}_{-0.9} \times 10^{23} \text{ cm}^{-2}$. Despite this large variation in column density, the fluxes of these two epochs are identical. This likely rules out changes where the absorber is only reacting to the continuum, via changes in ionisation and implies that the absorber variations are intrinsic and due to the column density. Finally we investigated if, in our best-fit models, there is any physical degeneracy between the column density, the ionisation or the outflow velocity. We therefore consider the *Suzaku* and the non-occulted part of the *XMM-Newton* & *NuSTAR* observations and allowed also the ionisation to be independent. In Figure 4 (upper panel) we show the confidence contours obtained for the ionisation

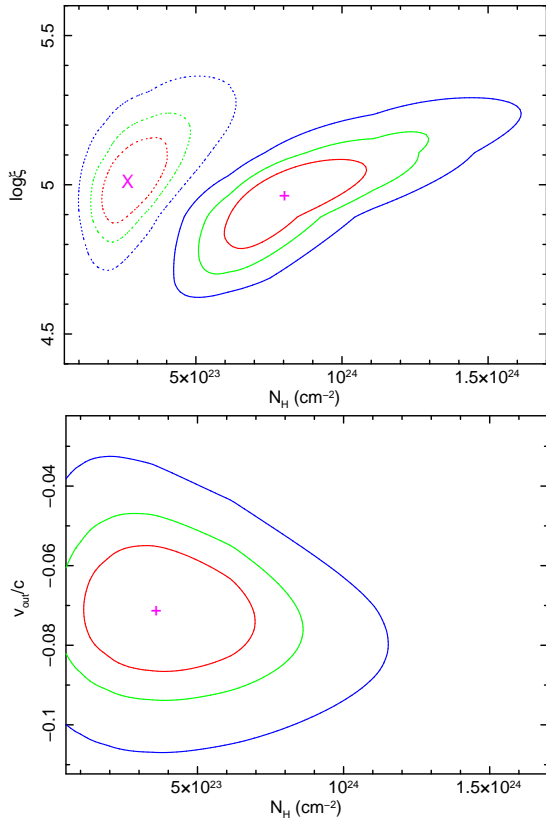


Figure 4. Upper Panel: contour plots for the ionisation against the N_H for the slow component of the disk wind in the *Suzaku* (solid lines) and the *XMM-Newton* & *NuSTAR* slice A spectra (dotted lines). This clearly demonstrates the variability of this zone in the $\log \xi$ - N_H plane. Lower Panel: contour plots for the disk wind velocity against the N_H for the *Swift* observation. The red, green and blue lines correspond to the 68%, 90% and 99% confidence levels for two interesting parameters.

versus the N_H for both these observations. Although the elongated shape of the contours suggests some degeneracy between $\log \xi$ and N_H , it is clear that the inferred variability of the opacity of this zone of the wind does not depend on the assumption of a constant ionisation. For the *Chandra* and *Swift* observations, since the ionisation is poorly constrained, we investigated the dependence of the N_H and the wind velocity. The relative contours for the *Swift* spectrum are shown in Figure 4 (lower panel).

3.3 Faster outflow components

Regarding the second fast zone, responsible for the 8.5 keV absorption feature, the fit substantially improves only for the *Suzaku* ($\Delta\chi^2/\Delta\nu = 35.0/2$) and *Swift* ($\Delta\chi^2/\Delta\nu = 10.0/2$) observations. Note that in both cases the fit improvement indicates that this zone is required at a $> 99.9\%$ confidence level. There is no evidence for this zone in the *Chandra* spectrum, where we are able to derive a rather stringent upper limit for the N_H of this faster zone of $N_H < 1.5 \times 10^{23} \text{ cm}^{-2}$. We found that the column density and outflow velocity ($v_{\text{out}2}/c \sim -0.2$; see Table 2) of this zone are rather similar between the 2010 and 2018 observations, suggesting that our line of sight intercepts a similar inner zone in both observing periods. In Fig. 5 we compare the *Suzaku*, *Chandra* and *Swift* spectra and the best fit models. It is noticeable that during the *Swift* observation the faster zone is similar to the fast zone detected in 2010. It is also

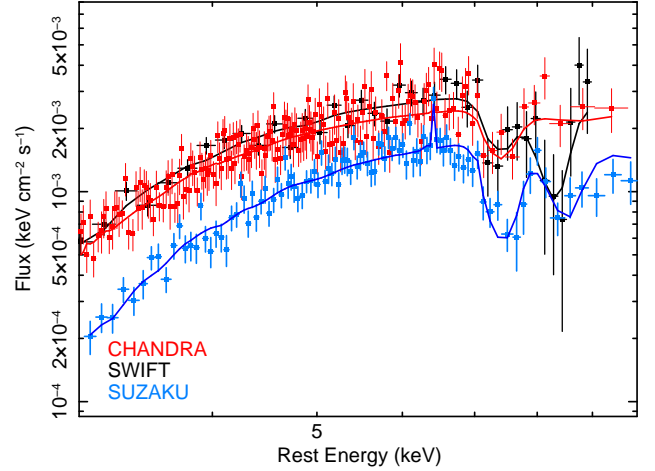


Figure 5. Best fit model and spectra for the *Swift* (black data points), *Chandra* (red data points) and *Suzaku* (light blue) observations. The model includes two ionized and outflowing absorbers, for which we assumed the same ionisation, but we allow the column densities to vary. Note that a deep absorption trough at ~ 7.3 keV is seen in all the observations, while the second and deeper ($EW \sim 300$ eV) structure at ~ 8.5 keV is detected only in the *Swift* and *Suzaku* observation. The *Swift* data were rebinned to adopting a constant energy binning of 150 eV for plotting purposes.

clear that such a zone is not present during the *Chandra* observation, despite that it caught MCG-03-58-007 at a similar flux level as seen in the 2018 *Swift* campaign.

As already discussed in B18 and M19, an even faster zone could be present during the 2015 *NuSTAR* observation ($\Delta\chi^2/\Delta\nu = 36.2/2$) with an outflowing velocity of $v_{\text{out}3}/c = -0.35 \pm 0.01$ and an $N_H = (3.8 \pm 1.2) \times 10^{23} \text{ cm}^{-2}$. In contrast to what was assumed in the previous works, here the ionisation of this zone was tied to the ionisation of the slow component. We note that the assumed value is within the errors of the $\log \xi$ previously reported. The imprint of this zone is the absorption structure seen in the *NuSTAR* spectra at around 10 keV (see Fig. 8 of B18); thereby we cannot assess if it is a persistent or sporadic streamline as it cannot be detected in the other observations, which lack the higher energy bandpass required to detect it.

4 DISCUSSION

We have presented the analysis of the current X-ray observations of the disk wind in MCG-03-58-007. Here, multiple and variable wind components with velocities ranging from $\sim -0.08 c$ to $\sim -0.2 c$ (and potentially up to $0.35 c$) are seen at different times. Multi epoch observations of disk winds, like the one presented here, are crucial for revealing all the possible phases of the disk wind. For example, over a decade worth of observations of PDS 456 revealed that the wind is most likely clumpy and/or stratified with the ionisation ranging from $\log(\xi/\text{erg cm s}^{-1}) \sim 2 \text{ erg cm s}^{-1}$ up to $\log(\xi/\text{erg cm s}^{-1}) = 6 \text{ erg cm s}^{-1}$ and velocities ranging from $\sim -0.2 c$ up to $\sim -0.46 c$ (Reeves et al. 2016, 2018a, 2020). It is possible, as suggested in other examples of ultra fast disk winds, that we are looking at a stratified wind, where multiple components are launched at different disk radii, but not all of them are always detected. This adds MCG-03-58-007 to the small but growing list of multiphase fast X-ray winds. Other examples of AGN with at least two variable

Table 2. Summary of the two phase disk wind model applied to all the observations. ^a: the normalisation units are 10^{-3} ph keV $^{-1}$ cm $^{-2}$. ^b: The *XMM-Newton* & *NuSTAR* 2015 slice A and slice B spectra were fitted simultaneously. ^c: We performed a joint fit of the *Chandra* and *Swift* spectra, because MCG-03-58-007 was in a similar flux state. ^t: denotes parameter was tied. ^f: denotes that the parameter was fixed. The fluxes are corrected only for the Galactic absorption, while the luminosities are intrinsic.

| Model Component | Parameter | <i>Suzaku</i> | Slice A | Slice B | <i>Chandra</i> | <i>Swift</i> |
|-------------------|--|--|--|---|--|---|
| Primary Power-law | Γ | 2.17 ^f | 2.17 ^{+0.06} _{-0.06} | 2.17 ^t | 2.17 ^f | 2.17 ^f |
| | Norm. ^a | 3.1 ^{+0.2} _{-0.2} | 2.6 ^{+0.3} _{-0.3} | 1.5 ^{+0.2} _{-0.2} | 4.4 ^{+0.2} _{-0.2} | 4.9 ^{+0.3} _{-0.3} |
| Neutral absorber | $N_{\text{H}}(\times 10^{23} \text{ cm}^{-2})$ | 2.7 ^{+0.1} _{-0.1} | 2.2 ^{+0.1} _{-0.1} | 2.2 ^t | 2.0 ^{+0.1} _{-0.1} | 1.9 ^{+0.1} _{-0.1} |
| Zone 1 | $N_{\text{H}1}(\times 10^{23} \text{ cm}^{-2})$ | 8.1 ^{+3.0} _{-2.4} | 2.6 ^{+1.1} _{-0.9} | 5.0 ^{+2.2} _{-1.3} | 3.6 ^{+2.4} _{-2.1} | 3.7 ^{+3.6} _{-2.8} |
| | $\log \xi_1$ | 5.0 ^{+0.1} _{-0.2} | 5.0 ^f | 3.70 ^{+0.11} _{-0.16} | 5.0 ^f | 5.0 ^f |
| | $v_{\text{out}1}/c$ | -0.077 ^{+0.009} _{-0.009} | -0.073 ^{+0.022} _{-0.022} | -0.13 ^{+0.02} _{-0.02} | -0.072 ^{+0.017} _{-0.017} | -0.072 ^t |
| | $\Delta\chi^2/\Delta\nu$ | 107.5/3 | 50.6/5 ^b | | 17.3/3 ^c | |
| Zone 2 | $N_{\text{H}2}(\times 10^{23} \text{ cm}^{-2})$ | 6.0 ^{+3.1} _{-2.2} | 3.8 ^{+1.2} _{-1.2} | 3.8 ^t | < 1.5 | 7.0 ^{+5.6} _{-4.1} |
| | $\log \xi_2$ | 5.0 ^t | 5.0 ^t | 5.0 ^t | 5.0 ^t | 5.0 ^t |
| | $v_{\text{out}2}/c$ | -0.20 ^{+0.02} _{-0.02} | -0.35 ^{+0.01} _{-0.01} | -0.35 ^t | -0.17 ^f | -0.17 ^{+0.03} _{-0.03} |
| | $\Delta\chi^2/\Delta\nu$ | 35.0/2 | 36.2/2 ^b | | 10.0/2 ^c | |
| | $F_{(2-10) \text{ keV}} \times 10^{12} \text{ (erg cm}^{-2} \text{ s}^{-1})$ | 2.0 | 2.1 | 1.0 | 3.8 | 3.6 |
| | $L_{(2-10) \text{ keV}} \times 10^{43} \text{ (erg s}^{-1})$ | 1.4 | 1.2 | 0.8 | 2.0 | 2.2 |
| χ^2/ν | | 230.1/202 | 468.2/395 ^b | | 339.7/340 ^c | |

phases of the X-ray winds are PG 1211+143 (Pounds et al. 2016; Reeves et al. 2018b), IRAS 13224-3809 (Chartas & Canas 2018; Parker et al. 2017; Pinto et al. 2018), 1H 0707-495 (Kosec et al. 2018), IRAS 17020+4544 (Longinotti et al. 2015) and PG 1114+445 (Serafinelli et al. 2019). In those cases, multiple phases with a common or different outflowing velocities are detected in the X-ray band. In contrast to most of the cases reported so far, neither of the two phases seen in MCG-03-58-007 requires a different ionisation (aside from slice B) suggesting that we are seeing different streamlines of the same highly ionized flow. The only exception could be the eclipsing event seen in 2015, where a solution is found with a lower ionisation for the Fe K intervening absorber. However, what we most likely see during this occultation event is a higher density and lower ionisation clump of the wind, which could be faster because its higher opacity makes it easier to accelerate (Waters et al. 2017). Note that this does not imply that the soft X-ray wind components, like the ones seen for example in PDS 456 or PG 1211+143, are not present; in contrast to the other examples, MCG-03-58-007 is seen through a relatively high column density ($N_{\text{H}} \sim 2 \times 10^{23} \text{ cm}^{-2}$, see Table 2) neutral absorber, therefore these phases may be hidden behind it. MCG-03-58-007 is not the only example where multiple Fe-K zones with the same ionisation and outflowing with different velocities had been detected in a single observation. For instance, two simultaneous Fe-K phases were detected at least twice in PDS456 (Reeves et al. 2018a, 2020) and possibly in PG 1211+143 (Pounds et al. 2016) and IRAS 13349+2438 (Parker et al. 2020).

We now discuss the properties of the various phases of the disk wind and the implications for the overall energetics. Evidently, if we want to understand the possible impact of the disk wind on the host galaxy, it is important not only to estimate the mass outflow rate and kinetic energy that the outflow can transport at a specific epoch, but also to account for all the phases of the wind and their variability. Crucially, what we need to establish is whether or not the

wind is persistent and if variable, its average kinetic energy. Overall, the wind detected in MCG-03-58-007 is at least composed by two variable zones: a persistent slow component with an outflow velocity of $v_{\text{out}1} \sim -0.08 c$ and a sporadic second faster zone with a velocity of $v_{\text{out}2} \sim -0.2 c$.

4.1 The slower outflow component

For the estimate of the outflow rates, we first concentrate on the lowest velocity zone, because it is clear that this phase (zone 1) is persistent as it is detected in all the observations analysed so far. We note that this zone shows an extreme variability with both long and short term variations of the N_{H} , suggesting that the wind is inhomogeneous. While the N_{H} of this zone varies among the different epochs, the velocity appears to be constant within the errors (see Table 2, slice B excepted). In particular, while the hard X-ray luminosity varies by a factor of ~ 2.8 (see Table 2), the wind does not appear to directly respond to it in either velocity or ionization. Our interpretation is that we are most likely seeing the same component, which is always present but clumpy as indeed we have already witnessed an occultation event, when during slice B our line of sight intercepted a higher opacity clump of the wind (see Table 2).

The crucial parameter needed to infer the energetics of the disk wind is its mass outflow rate dM/dt (\dot{M}_{out}). This can be derived using the equation (see Nardini et al. 2015):

$$\dot{M}_{\text{out}} = \Omega \mu m_p v_{\text{out}} R_w N_{\text{H}} \quad (1)$$

where μ is a constant factor set to $\mu = n_{\text{H}}/n_{\text{e}} = 1.2$ for solar abundances, Ω is the wind solid angle, R_w is the disk wind radius, N_{H} and v_{out} are the column density and the velocity of the disk wind. Since we do not know the exact geometry for MCG-03-58-007,

following the same argument presented in [Gofford et al. \(2015\)](#) and [Tombesi et al. \(2013\)](#), we assumed that the wind subtends $\Omega/4\pi = 0.5$. Indeed, the systematic search of fast disk winds in bright nearby local AGN resulted in a detection rate of about 40%, suggesting these winds have a wide opening angle. Note that a large solid angle of about 2π was derived for the wind in PDS 456 from its P-Cygni Fe K profile ([Nardini et al. 2015](#)).

The main parameter that we now need to quantify is the launching radius of the wind; a lower limit of the radial distance can be derived from the outflow velocity assuming that the wind is launched at its escape radius $R_{\min} = 2 G M_{\text{BH}}/v^2$. We note that by adopting this radius, we derive the most conservative estimate of the mass outflow rate and energetics (see [Gofford et al. 2013](#); [Tombesi et al. 2012](#)). As the main uncertainty in this latter equation is the black hole mass of MCG-03-58-007, we decided to normalise the mass outflow rate to the Eddington rate:

$$\dot{M}_{\text{Edd}} = 4\pi G m_p M_{\text{BH}} / \sigma_T \eta c \quad (2)$$

where σ_T is the Thomson cross section and $\eta = 0.1$ is the accretion efficiency. Thus combining equation (1) and (2) and substituting for R_{\min} we obtain:

$$\dot{M} = \frac{\dot{M}_{\text{out}}}{\dot{M}_{\text{Edd}}} = 2 \frac{\Omega}{4\pi} \mu N_H \sigma_T \eta \left(\frac{v_{\text{out}}}{c} \right)^{-1} \quad (3)$$

The kinetic power ($L_{\text{KIN}} = 1/2 \dot{M}_{\text{out}} v_{\text{out}}^2$) of the wind can also be normalised to the Eddington luminosity ($L_{\text{Edd}} = \eta \dot{M}_{\text{Edd}} c^2$). Thus substituting for \dot{M}_{out} and \dot{M}_{Edd} the wind kinetic power is:

$$\dot{E} = \frac{L_{\text{KIN}}}{L_{\text{Edd}}} = \frac{\Omega}{4\pi} \mu N_H \sigma_T \frac{v_{\text{out}}}{c} \quad (4)$$

In Table 3 we report the resulting values for all the phases of the X-ray wind; there we list the outflow rate (\dot{M}) and the kinetic output (\dot{E}) of the wind normalised to the Eddington rates. The errors are calculated by propagating the 90% errors on the column density and velocity of the disk wind (see Table 2). It is clear that the wind seen during the *Suzaku* observation, with a higher \dot{M} and \dot{E} , is much stronger than during the *XMM-Newton* slice A. On the other hand, the wind seen in the *Chandra* and *Swift* spectra, because of the large errors, could be consistent with either of the two previous epochs. While all the derived \dot{M} are a substantial fraction of the Eddington rate, the \dot{E} are typically constrained in MCG-03-58-007 to within 1-3% of Eddington, in line with the typical estimates for powerful winds in other AGN (e.g. [Gofford et al. 2015](#)).

In order to compare the disk wind kinematics with the ones reported for the possible kpc-scale molecular outflow ([Sirressi et al. 2019](#)), we considered the values obtained for the persistent component (zone 1) and converted the \dot{E} to the absolute values of the kinetic output by adopting the estimated black hole mass of MCG-03-58-007 of $M_{\text{BH}} \sim 10^8 M_{\odot}$ (see B18 and [Sirressi et al. 2019](#)). The kinetic power of this zone ranges from $L_{\text{KIN}} \sim 10^{44} \text{ erg s}^{-1}$, as measured during the first part of the *XMM-Newton* observations, to $\sim 3 \times 10^{44} \text{ erg s}^{-1}$ for the *Suzaku* observation (see Table 3). Thus on average the derived kinetic output of this zone is of the order of $L_{\text{KIN}} \sim 1.7 \times 10^{44} \text{ erg s}^{-1}$, which is $\sim 5\% L_{\text{bol}}$, where the bolometric luminosity of MCG-03-58-007 is $L_{\text{bol}} \sim 3 \times 10^{45} \text{ erg s}^{-1}$ (B18). Regardless of the N_H variability, all the estimates of the kinetic energy of the X-ray wind are at least two orders of magnitude above the kinetic energy carried by the molecular gas phase (with $\dot{E}_{\text{CO}}/\dot{E}_X$ ranging from $\sim 3 \times 10^{-3}$ to $\sim 10^{-2}$; [Sirressi et al. 2019](#)). Note

that, despite the large errors on the N_H and the uncertainties on the black hole mass, we cannot reconcile the different measurements of the X-ray wind energetics versus the large scale CO wind. Even if we consider the lowest possible measurement of $\dot{E} \sim 0.003$ (e.g. the 90% lower value for the *Swift* observation, see Table 3) we derive $L_{\text{KIN}} \sim 3.8 \times 10^{43} \text{ erg s}^{-1}$. Therefore we would need a ~ 40 times smaller black hole mass (e.g. $M_{\text{BH}} \sim 5 \times 10^6 M_{\odot}$) to have $L_{\text{KIN}} \sim 10^{42} \text{ erg s}^{-1}$ in order to be compatible with the CO wind kinetic power. This is implausible, because such a low black hole mass would make MCG-03-58-007 a super Eddington source, given its bolometric luminosity of $L_{\text{bol}} \sim 3 \times 10^{45} \text{ erg s}^{-1}$.

The momentum rate of the X-ray wind is $\dot{p}_{\text{out}} = \dot{M}_{\text{out}} v_{\text{out}}$; here \dot{p}_{out} was calculated again by adopting $M_{\text{BH}} \sim 10^8 M_{\odot}$. The momentum rates of the disk wind listed in Table 3 are all normalised to the momentum rate of the radiation $\dot{p}_{\text{rad}} = L_{\text{bol}}/c$. Hence the X-ray wind momentum rate ranges from $\dot{p}/\dot{p}_{\text{rad}} \sim 0.9$ (slice A) to ~ 2.7 (*Suzaku* observation). Although these estimates are clearly affected by large uncertainties, the momentum rates derived in each of the observations is of the same order of the radiation momentum rate (see Table 3), suggesting that this stream of the wind could be radiation driven with only a moderate force multiplier.

We note that the momentum rate of the molecular outflow is consistent with that of the X-ray wind suggesting that the outflow is more likely to be momentum rather than energy conserving on large scales. A similar scenario also applies to other powerful X-ray winds such as PDS 456 ([Bischetti et al. 2019](#)), IZw 1 ([Reeves & Braito 2019](#)), IRAS F11119 + 3257 ([Veilleux et al. 2017](#); [Nardini & Zubovas 2018](#)) and the high redshift QSO, APM 08279 + 5255 ([Feruglio et al. 2017](#)). We note that recent hydrodynamical simulations of small scale winds in galaxies predict larger scale energy conserving winds, because the Compton cooling times are expected to be short compared to the dynamical times of the inner winds ([Costa et al. 2020](#)), meaning the solely momentum-driven wind can hardly happen. It is possible that a more energetic large scale outflow is present in MCG-03-58-007, but it is ionized rather than molecular gas. Interestingly, in the optical spectrum from the 6dF Galaxy Survey (6dFGS, [Jones et al. 2009](#)), there is evidence for possible blue wings in the profiles of the [O III] $\lambda 4959, \lambda 5007 \text{ \AA}$ emission lines blue-shifted by $v_{\text{out}} \sim 500 \text{ km s}^{-1}$; unfortunately from the currently available spectrum we cannot derive an estimate on the morphology and energetics of this possible ionised large scale outflow. Future spatially resolved optical spectroscopy using the VLT Multi-Unit Spectroscopic Explorer (MUSE) could reveal the structure and kinematics of this ionised component of the large scale outflow and provide an estimate its energetics, which could then be compared with the X-ray and large scale molecular winds.

We would like to stress the following consideration; had we not witnessed that the slice B spectrum is due to a rare occultation event, as if for example this was the only observation of the wind, we would have inferred an incomplete picture of the disk wind. First of all, we note that with the finer grid we now measure a less extreme wind parameters of $\dot{M} \sim 0.31$ and $\dot{E} \sim 0.026$, which are similar to the values measured during the *Suzaku* observation. However, if the wind is at the escape radius, which can be derived from $v_{\text{out}} \sim 0.13 c$ ($R \sim 10^{15} \text{ cm}$), its ionisation should be higher, of the order of $\log(\xi/\text{erg cm s}^{-1}) \sim 5$. This can be derived using the relation

Table 3. Summary of the energetics of the different phases of the disk wind. ^a: Mass outflow rate (\dot{M}) in Eddington units. ^b: Here zone 2 refers to the faster zones seen outflowing at $v \sim -0.2c$ in the *Suzaku* and *Swift* observations and at $v \sim -0.35c$ in the *XMM-NuSTAR* observation, respectively. ^c: Outflow kinetic power (\dot{E}) in Eddington units ^d: The kinetic power unit is erg s^{-1} and is derived for $M_{\text{BH}} = 10^8 M_{\odot}$. ^e: The outflow energetics for the molecular gas depends on the CO-to- H_2 conversion factor, here a factor of $2.1 M_{\odot} (\text{K km s}^{-1} \text{ pc}^2)^{-1}$ was adopted (Sirressi et al. 2019).

| Observation | parameter | zone 1 ^a | zone 2 ^b |
|--------------------------------|---|---------------------------|---------------------------|
| <i>Suzaku</i> 2010 | \dot{M} | $0.84^{+0.33}_{-0.27}$ | $0.24^{+0.13}_{-0.09}$ |
| | \dot{E}^c | $0.025^{+0.01}_{-0.008}$ | $0.048^{+0.025}_{-0.018}$ |
| | $\log L_{\text{KIN}}^d$ | 44.5 | 44.8 |
| | $\dot{p}_w (L_{\text{bol}}/c)$ | 2.7 | 2.0 |
| <i>XMM-NuSTAR</i> 2015 slice A | \dot{M} | $0.28^{+0.15}_{-0.12}$ | $0.09^{+0.03}_{-0.03}$ |
| | \dot{E} | $0.008^{+0.004}_{-0.004}$ | $0.053^{+0.017}_{-0.017}$ |
| | $\log L_{\text{KIN}}$ | 44.0 | 44.8 |
| | $\dot{p}_w (L_{\text{bol}}/c)$ | 0.9 | 1.0 |
| <i>Chandra</i> 2016 | \dot{M} | $0.40^{+0.28}_{-0.25}$ | < 0.07 |
| | \dot{E} | $0.010^{+0.007}_{-0.006}$ | < 0.01 |
| | $\log L_{\text{KIN}}$ | 44.1 | < 44 |
| | $\dot{p}_w (L_{\text{bol}}/c)$ | 1.2 | < 0.5 |
| <i>Swift</i> 2018 | \dot{M} | $0.41^{+0.41}_{-0.33}$ | $0.33^{+0.27}_{-0.20}$ |
| | \dot{E} | $0.011^{+0.011}_{-0.008}$ | $0.047^{+0.038}_{-0.029}$ |
| | $\log L_{\text{KIN}}$ | 44.1 | 44.8 |
| | $\dot{p}_w (L_{\text{bol}}/c)$ | 1.2 | 2.3 |
| ALMA ^d | $\dot{M}_{\text{out}} (M_{\odot} \text{yr}^{-1})$ | 54 | |
| ALMA | $\log E_{\text{CO}}$ | 42 | |
| ALMA | $\dot{p}_{\text{CO}} (L_{\text{bol}}/c)$ | 0.8 | |

$R^2 = L_{\text{ion}}/n_e \xi$ ³ assuming that the size of the absorber is $\Delta R/R = 0.1$. However, if we adopt the more realistic location of the wind of $R \sim 10^{16} \text{ cm}$, as derived by B18 from the absorption variability, we infer a much higher mass outflow rate ($\dot{M}_{\text{out}} \sim 4 M_{\odot}/\text{yr}$). The kinetic output would be of the order of 10% of L_{Edd} . These more extreme values are likely implausible and the transient nature of the slice B absorption suggests that this is due to a passing wind clump of higher than usual density (and consequently lower ionisation). Such clumps likely have a lower filling factor which is confirmed by the fact that this state is seen only once among all the 11 observations (see Table 1) that we have for MCG-03-58-007. We note that no spectral variability was seen amongst all the *Swift* observations, whereas an obscuration event like the one seen in slice B, would have been easily detected. In particular, although we could not characterise the wind in each of the short *Swift* observations, we would have been able to detect the strong curvature imprinted by this denser patch in the 3-6 keV band. This stresses even more the importance of multi epoch observations to understand the nature of the X-ray winds.

4.2 Faster outflow components

Regarding the two faster zones of the X-ray wind, which are outflowing with $v_{\text{out}2} \sim -0.2c$ and with $v_{\text{out}3} \sim -0.35c$, a possible scenario is that they are innermost streamlines of the wind closer to the black hole. In the discussion below, we concentrate on the $0.2c$ outflow, which has been independently confirmed in two of the observations.

For the component outflowing with $v_{\text{out}2} \sim -0.2c$, from its velocity we can infer that this zone is most likely launched at a distance of $R_{w2} \sim 7.5 \times 10^{14} \text{ cm}$ (or $\sim 50 R_g$); this implies that the density has to be of the order of $n_e \sim 10^{10} \text{ cm}^{-3}$ so that the iron is not fully ionized and we are able to detect it. This in turn implies a rather small size scale for the streamline or clumps of the wind of $\Delta R = N_{\text{H}}/n_e \sim 10^{14} \text{ cm}$, which is comparable to the X-ray source size ($\sim 10 R_g$). Thanks to the multi epochs observations, it is now clear that zone 2 is sporadic; indeed, we can place a rather stringent upper limit on the N_{H} of this zone to be less than $1.5 \times 10^{23} \text{ cm}^{-2}$ during the *Chandra* observation (see Fig. 5).

The appearance of this zone seems to be irregular and uncorrelated to the X-ray luminosity. A possible scenario is that this faster zone is always present but, being launched from closer in, is generally more ionized and we are able to detect it only when our line of sight intercepts, like in slice B, a denser and/or lower ionisation clumps. Alternatively it is possible that this inner streamline corresponds to different ejecta events. In terms of its energetics, while its mass outflow rate is smaller or comparable to the mass carried by the slower phase of the wind, the kinetic output is higher given the higher velocity and could be of the order of $\sim 6 \times 10^{44} \text{ erg s}^{-1}$, which correspond to $\sim 20\%$ of L_{bol} . Taken at face value this would imply that this phase could be even more important in terms of the feedback on the host galaxy. Nonetheless, as this phase could be intermittent, the derived kinetic output, although apparently high, may not be important in terms of its feedback as the fast component could be a short lived phase.

We have very recently performed a new series of four simultaneous *XMM-Newton* & *NuSTAR* observations of MCG-03-58-007, covering a time period of a month, that will allow us to probe the short term

³ where L_{ion} is the ionising luminosity in the 1-1000 Rydberg range ($L_{\text{ion}} \sim 10^{45} \text{ erg s}^{-1}$ as derived in B18) and n_e is density of the gas

variability of the wind and if and how it reacts to changes of the X-ray source luminosity. These observations will crucially allow us also to probe the connection between the two faster zones of the wind (Braito et al. in prep.).

5 ACKNOWLEDGEMENTS

We thank the referee for his/her useful comments that improved the paper. This research has made use of data obtained from *Suzaku*, a collaborative mission between the space agencies of Japan (JAXA) and the USA (NASA). Based on observations obtained with *XMM-Newton*, an ESA science mission with instruments and contributions directly funded by ESA Member States and the USA (NASA). This work is based on observations obtained with the Neil Gehrels *Swift* Observatory. This work has been partially supported by the ASI-INAF program I/004/11/4. This work made use of data from the *NuSTAR* mission, a project led by the California Institute of Technology, managed by the Jet Propulsion Laboratory, and funded by NASA. This research has made use of the NuSTAR Data Analysis Software (NuSTARDAS) jointly developed by the ASI Science Data Center and the California Institute of Technology. VB acknowledges financial support through the NASA grant 80NSSC20K0793 and the Chandra grant GO7-18091X. VB, RDC, PS and RS acknowledge financial contribution from the agreements ASI-INAF n.2017-14-H.O. GAM is supported by ESA research fellowships.

6 DATA AVAILABILITY

The data used for this research can be accessed at <https://heasarc.gsfc.nasa.gov/docs/archive.html>.

REFERENCES

- Bischetti, M., Piconcelli, E., Feruglio, C., et al. 2019, *A&A*, 628, A118
 Braito, V., Reeves, J. N., Matzeu, G. A., et al. 2018, *MNRAS*, 479, 3592
 Chartas, G., Brandt, W. N., Gallagher, S. C., & Garmire, G. P. 2002, *ApJ*, 579, 169
 Chartas, G., & Canas, M. H. 2018, *ApJ*, 867, 103
 Cicone, C., Maiolino, R., Sturm, E., et al. 2014, *A&A*, 562, A21
 Cicone, C., Maiolino, R., Gallerani, S., et al. 2015, *A&A*, 574, A14
 Costa, T., Pakmor, R., & Springel, V. 2020, arXiv e-prints, arXiv:2006.05997
 Dickey, J. M., & Lockman, F. J. 1990, *ARA&A*, 28, 215
 Di Matteo, T., Springel, V., & Hernquist, L. 2005, *Nature*, 433, 604
 Faucher-Giguère, C.-A., & Quataert, E. 2012, *MNRAS*, 425, 605
 Fiore, F., Feruglio, C., Shankar, F., et al. 2017, *A&A*, 601, A143
 Fruscione, A., McDowell, J. C., Allen, G. E., et al. 2006, *Proc. SPIE*, 6270, 62701V
 Ferrarese, L., & Merritt, D. 2000, *ApJ*, 539, L9
 Feruglio, C., Fiore, F., Carniani, S., et al. 2015, *A&A*, 583, A99
 Feruglio, C., Ferrara, A., Bischetti, M., et al. 2017, *A&A*, 608, A30
 Fukumura, K., Kazanas, D., Contopoulos, I., & Behar, E. 2010, *ApJ*, 715, 636
 Fukumura, K., Kazanas, D., Shrader, C., et al. 2017, *Nature Astronomy*, 1, 0062
 Gandhi, P., Horst, H., Smette, A., et al. 2009, *A&A*, 502, 457
 Garmire, G. P., Bautz, M. W., Ford, P. G., Nousek, J. A., & Ricker, G. R., Jr. 2003, *Proc. SPIE*, 4851, 28
 Gebhardt, K., Bender, R., Bower, G., et al. 2000, *ApJ*, 539, L13
 Giustini, M., & Proga, D. 2012, *ApJ*, 758, 70
 Gofford, J., Reeves, J. N., Tombesi, F., et al. 2013, *MNRAS*, 430, 60
 Gofford, J., Reeves, J. N., McLaughlin, D. E., et al. 2015, *MNRAS*, 451, 4169
 Harrison, F. A., Craig, W. W., Christensen, F. E., et al. 2013, *ApJ*, 770, 103
 Jones, D. H., Read, M. A., Saunders, W., et al. 2009, *MNRAS*, 399, 683
 Hopkins, P. F., & Elvis, M. 2010, *MNRAS*, 401, 7
 Kallman, T. R., Palmeri, P., Bautista, M. A., Mendoza, C., & Krolik, J. H. 2004, *ApJS*, 155, 675
 Kato, Y., Mineshige, S., & Shibata, K. 2004, *ApJ*, 605, 307
 Kazanas, D., Fukumura, K., Behar, E., Contopoulos, I., & Shrader, C. 2012, *The Astronomical Review*, 7, 92
 King, A. R., & Pounds, K. A. 2003, *MNRAS*, 345, 657
 King, A. R. 2010, *MNRAS*, 402, 1516
 King, A. R., Zubovas, K., & Power, C. 2011, *MNRAS*, 415, L6
 King, A., & Pounds, K. 2015, *ARA&A*, 53, 115
 Kosec, P., Buisson, D. J. K., Parker, M. L., et al. 2018, *MNRAS*, 481, 947
 Krongold, Y., Nicastro, F., Elvis, M., et al. 2007, *ApJ*, 659, 1022
 Longinotti, A. L., Krongold, Y., Guainazzi, M., et al. 2015, *ApJ*, 813, L39
 Longinotti, A. L., Vega, O., Krongold, Y., et al. 2018, *ApJ*, 867, L11
 Magorrian, J., Tremaine, S., Richstone, D., et al. 1998, *AJ*, 115, 2285
 Mitsuda, K., et al. 2007, *PASJ*, 59, 1
 Matzeu, G. A., Reeves, J. N., Braito, V., et al. 2017, *MNRAS*, 472, L15
 Matzeu, G. A., Braito, V., Reeves, J. N., et al. 2019, *MNRAS*, 483, 2836
 Mewe, R., Gronenschild, E. H. B. M., & van den Oord, G. H. J. 1985, *A&AS*, 62, 197
 Mizumoto, M., Izumi, T., & Kohno, K. 2019, *ApJ*, 871, 156
 Murphy, K. D., & Yaqoob, T. 2009, *MNRAS*, 397, 1549
 Nandra, K., O'Neill, P. M., George, I. M., & Reeves, J. N. 2007, *MNRAS*, 382, 194
 Nardini, E., Reeves, J. N., Gofford, J., et al. 2015, *Science*, 347, 860
 Nardini, E., & Zubovas, K. 2018, *MNRAS*, 478, 2274
 Parker, M. L., Pinto, C., Fabian, A. C., et al. 2017, *Nature*, 543, 83
 Parker, M. L., Matzeu, G. A., Alston, W. N., et al. 2020, *MNRAS*, 498, L140
 Pinto, C., Alston, W., Parker, M. L., et al. 2018, *MNRAS*, 476, 1021
 Pounds, K. A., Reeves, J. N., King, A. R., et al. 2003, *MNRAS*, 345, 705
 Pounds, K., Lobban, A., Reeves, J., et al. 2016, *MNRAS*, 457, 2951
 Proga, D., Stone, J. M., & Kallman, T. R. 2000, *ApJ*, 543, 686
 Proga, D., & Kallman, T. R. 2004, *ApJ*, 616, 688
 Reeves, J. N., O'Brien, P. T., & Ward, M. J. 2003, *ApJ*, 593, L65
 Reeves, J. N., O'Brien, P. T., Braito, V., et al. 2009, *ApJ*, 701, 493
 Reeves, J. N., Braito, V., Gofford, J., et al. 2014, *ApJ*, 780, 45
 Reeves, J. N., Braito, V., Nardini, E., et al. 2016, *ApJ*, 824, 20
 Reeves, J. N., Braito, V., Nardini, E., et al. 2018a, *ApJ*, 854, L8
 Reeves, J. N., Lobban, A., & Pounds, K. A. 2018b, *ApJ*, 854, 28
 Reeves, J. N., & Braito, V. 2019, *ApJ*, 884, 80
 Reeves, J. N., Braito, V., Chartas, G., et al. 2020, *ApJ*, 895, 37
 Saez, C., & Chartas, G. 2011, *ApJ*, 737, 91
 Serafinelli, R., Tombesi, F., Vagnetti, F., et al. 2019, *A&A*, 627, A121
 Sim, S. A., Long, K. S., Miller, L., & Turner, T. J. 2008, *MNRAS*, 388, 611
 Sim, S. A., Proga, D., Miller, L., Long, K. S., & Turner, T. J. 2010, *MNRAS*, 408, 1396
 Sirressi, M., Cicone, C., Severgnini, P., et al. 2019, *MNRAS*, 489, 1927
 Tombesi, F., Cappi, M., Reeves, J. N., et al. 2010, *A&A*, 521, A57
 Tombesi, F., Cappi, M., Reeves, J. N., & Braito, V. 2012, *MNRAS*, 422, L1
 Tombesi, F., Cappi, M., Reeves, J. N., et al. 2013, *MNRAS*, 430, 1102
 Tombesi, F., Meléndez, M., Veilleux, S., et al. 2015, *Nature*, 519, 436
 Tombesi, F., Veilleux, S., Meléndez, M., et al. 2017, *ApJ*, 850, 151
 Veilleux, S., Bolatto, A., Tombesi, F., et al. 2017, *ApJ*, 843, 18
 Waters, T., Proga, D., Dannen, R., et al. 2017, *MNRAS*, 467, 3160
 Wilms, J., Allen, A., & McCray, R. 2000, *ApJ*, 542, 914
 Zubovas, K., & King, A. 2012, *ApJ*, 745, L34
 Zubovas, K., & King, A. 2016, *MNRAS*, 462, 4055